

Landau-Zener-Stückelberg-Majorana interferometry of a single hole

Alex Bogan, Sergei Studenikin,* Marek Korkusinski, Louis Gaudreau, Piotr Zawadzki, and Andy S. Sachrajda†
Emerging Technology Division, National Research Council, Ottawa, Canada, K1A0R6

Lisa Tracy
Sandia National Laboratories, Albuquerque, New Mexico 87185, USA

John Reno and Terry Hargett
Center for Integrated Nanotechnologies, Sandia National Laboratories, Albuquerque, New Mexico 87185, USA
(Dated: November 10, 2017)

We perform Landau-Zener-Stückelberg-Majorana (LZSM) spectroscopy on a system with strong spin-orbit interaction (SOI), realized as a single hole confined in a gated double quantum dot. In analogy to the electron systems, at magnetic field $B = 0$ and high modulation frequencies we observe the photon-assisted tunneling (PAT) between dots, which smoothly evolves into the typical LZSM funnel-shaped interference pattern as the frequency is decreased. In contrast to electrons, the SOI enables an additional, efficient spin-flipping interdot tunneling channel, introducing a distinct interference pattern at finite B . Magneto-transport spectra at low-frequency LZSM driving show the two channels to be equally coherent. High-frequency LZSM driving reveals complex photon-assisted tunneling pathways, both spin-conserving and spin-flipping, which form closed loops at critical magnetic fields. In one such loop an arbitrary hole spin state is inverted, opening the way toward its all-electrical manipulation.

Currently there is interest in coherent control of individual spins in the context of quantum-dot-based quantum computing with spin qubits [1, 2]. In gated devices, the single-spin control is achieved with micromagnets [3–5] or nanoantennas [6–8], requiring complex device engineering. Alternative proposals envision rotating the spin of the moving carrier via the electrostatically modulated Rashba spin-orbit interaction (SOI) [9], which promises simpler designs and improved device scalability. In electronic quantum dot systems this electrical spin manipulation has been reported in gated GaAs [10, 11] and InAs devices [12, 13]. However, here the SOI magnitude is small, comparable to the strength of nuclear hyperfine interactions, but much smaller than the interdot tunneling coupling [14–17]. On the other hand, theoretical proposals involving holes [18, 19], motivated by predictions of suppressed hyperfine interactions with nuclear spins [20–30], are at very early stages of implementation. In silicon-based hole devices, both lateral [31, 32] and nanowire systems [33, 34], control of the hole spin via the electric dipole spin resonance and the spin Rabi oscillations have been demonstrated [35, 36]. In GaAs-based devices the anisotropies of the hole tunneling current in a magnetic field [37] and the zero in-plane g-factor [38] were traced to the presence of strong SOI. Signatures of a high rate of spin-flipping tunneling between the dots in a double dot have been detected in magneto-transport [38], but the consequences of strong SOI have not yet been studied at the single-hole level.

Here we use Landau-Zener-Stückelberg-Majorana (LZSM) interferometry to probe the dynamics of a single hole confined in a lateral double-dot device. This experimental technique has been used to study the co-

herent phenomena in a variety of physical systems, from atomic to superconducting [39]. In gated dots, LZSM involves applying microwave modulation to the detuning between the dots and measure the resulting tunnel current or charge configuration. It has been applied to study the dynamics and characterize quantitatively the coherence of electronic charge qubits [40–46]. We demonstrate that for a single hole at zero magnetic field the LZSM phenomena arise from a single tunneling channel, analogous to that of a single-electron system. We recover all interference features seen in electronic samples. In particular, we observe the smooth evolution of the photon-assisted tunneling (PAT) pattern at high driving frequencies to the characteristic funnel-shaped fringes at low frequencies. A dramatic change in the spectra is seen in a nonzero magnetic field, where at all driving frequencies we report the coexistence of interference features generated by two tunneling channels, one spin-conserving and one spin-flipping. High-frequency LZSM interferometry reveals that several microwave-assisted tunneling pathways may coexist for critical values of detuning and magnetic fields, offering novel regimes of control of the hybrid charge-spin system.

Figure 1(a) shows the gate layout of our GaAs lateral double dot [38, 47]. We confine precisely one hole in the resultant lateral confinement, and control electrically the charge state from $(n_L, n_R) = (1, 0)$ to $(0, 1)$, where $n_{L(R)}$ is the number of holes in the left-hand (right-hand) dot. In what follows we assume that the hole can be placed in each dot in two spin states, which results in four possible spin and charge configurations: $(\downarrow, 0)$, $(\uparrow, 0)$, $(0, \downarrow)$, and $(0, \uparrow)$. At zero magnetic field the two spinors in each dot are degenerate. Denoting the energies of $(1, 0)$ and

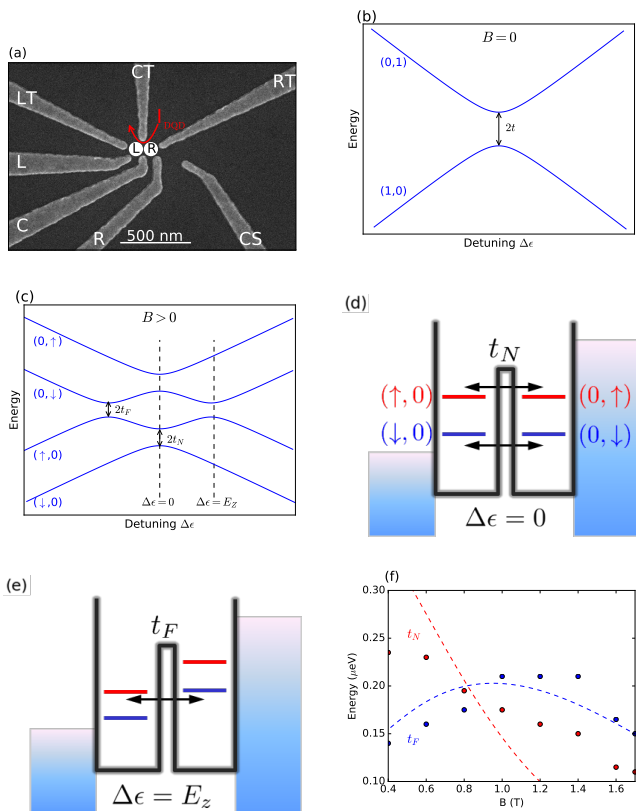


FIG. 1: (a) Layout of the gates creating the double-dot lateral confinement. The red arrow indicates the flow of the current I_{DOT} in the transport measurement. The yellow arrow denotes the current I_{CS} through the charge sensor CS . Panels (b) and (c) show the energy diagram of the system as a function of the detuning at zero and nonzero magnetic field, respectively. Panels (d) and (e) show schematic energy diagrams at a nonzero magnetic field, for the detuning equal zero and the Zeeman energy E_Z , respectively. Matrix elements t_N (t_F) characterize the spin conserving (flipping) tunneling resonance. (f) Magnitudes of the tunneling elements t_N (black) and t_F (red) as a function of the magnetic field extracted from experiment (symbols) and predicted by microscopic theory (dashed lines).

$(0, 1)$ charge configurations by ε_L and ε_R , respectively, the relative detuning $\Delta\varepsilon = \varepsilon_L - \varepsilon_R$ can be tuned by adjusting the voltage on the gate R. Figure 1(b) shows the energy diagram of the system as a function of $\Delta\varepsilon$. It consists of two degenerate energy levels, which anticross close to resonance, i.e., when $\Delta\varepsilon$ approaches zero, with the gap defined by the interdot tunneling rate t . This diagram is identical to that for double-dot with a single electron [40–46]. The dramatic differences can be seen at a finite magnetic field (Fig. 1(c)). Here, the different spin states of the same charge configuration are separated by the Zeeman energy E_Z . The states with the same spin exhibit anticrossings at $\Delta\varepsilon = 0$, as is the case for the electron, with the gaps defined by the spin-

conserving tunneling rate t_N . The alignment of dot levels corresponding to that resonance condition is visualized in Fig. 1(d), in which the spin-down (up) levels are represented with blue (red) bars. In our hole system, the strong SOI enables two additional large anticrossings occurring between the states with opposite spin, with gaps defined by the spin-flipping tunneling rate t_F . This element is due to the SOI [18, 19, 48, 49] and its microscopic form is established in Ref. [50]. The alignment of levels occurring at the detuning $\Delta\varepsilon = E_Z$ is shown schematically in Fig. 1(e). Here the left-dot spin-up level ($\uparrow, 0$) is resonant with the right-dot spin-down level ($0, \downarrow$) and we observe the coherent spin-flipping tunneling resonance.

Following Refs. [37, 48, 49], we describe our four-level system with the perturbative heavy-hole Hamiltonian, which in the presence of the magnetic field perpendicular to the dot surface is

$$\hat{H} = \begin{bmatrix} \varepsilon_L + E_Z/2 & 0 & -t_N & -it_F \\ 0 & \varepsilon_L - E_Z/2 & -it_F & -t_N \\ -t_N & it_F & \varepsilon_R + E_Z/2 & 0 \\ it_F & -t_N & 0 & \varepsilon_R - E_Z/2 \end{bmatrix}. \quad (1)$$

The Zeeman energy $E_Z = g^* \mu_B B$, where g^* is the effective hole g -factor, μ_B is the Bohr magneton, and B is the magnetic field. We have estimated the numerical values of the elements of the above Hamiltonian in magneto-transport spectroscopy by measuring the tunneling current, depicted in Fig. 1(a) with the red arrow, as a function of the detuning $\Delta\varepsilon$ and the magnetic field. We chose high source-drain voltage, corresponding to the alignment of Fermi energies of the leads as represented in Fig. 1(d), (e) by striped boxes. Following the procedure outlined in the supplementary material, Ref. [50], in Fig. 1(f) we show the extracted dependence of t_N and t_F on the magnetic field (red and black dots, respectively). We compare it qualitatively to the trends predicted by a simple microscopic model (red and black dashed lines, respectively). The spin-flipping tunneling element is of similar magnitude to that of the spin-conserving process, but the two elements differ in their dependence on the magnetic field. The element t_N decreases, while t_F first increases and then decreases as the field grows. The behavior of t_N is a consequence of the decreasing overlap between the left-dot and right-dot orbitals due to the tightening of the cyclotron orbits as the field grows. The complex dependence of t_F , on the other hand, is a direct consequence of the SOI nature of this element, as it depends on the orbital overlap as well as the momentum. As the field grows, the overlap between orbitals decreases, but the momentum obtains an increasing correction arising from the magnetic vector potential. The observed behaviour is a result of the interplay of these two trends. The characteristic increase of the spin-flipping tunneling element has been observed for electronic double dots [16].

The LZSM interferometry in magneto-transport is per-

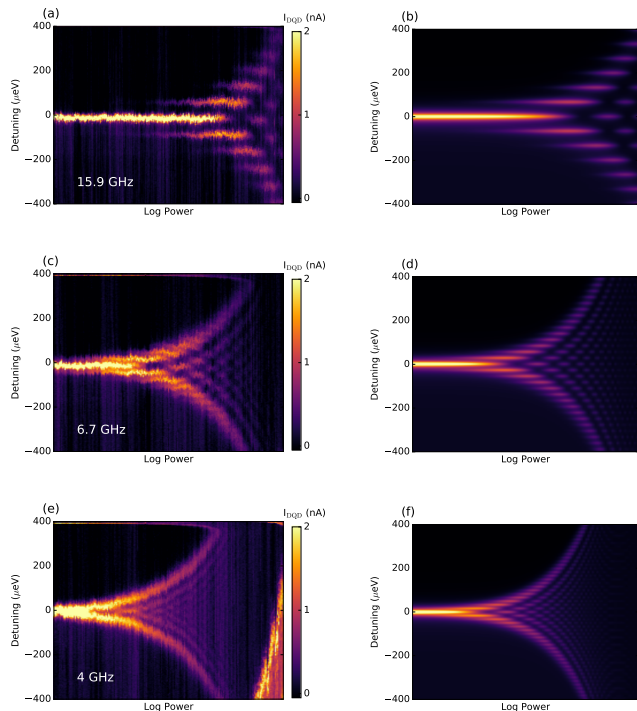


FIG. 2: LZSM interferometry of a single hole at zero magnetic field. Panels (a), (c), and (e) show the tunneling current measured as a function of detuning and microwave power at driving frequencies 15.9 GHz, 6.7 GHz, and 4 GHz, respectively. Panels (b), (d), and (f) show respectively the results of model calculations at matching conditions.

formed by applying a sinusoidal microwave modulation to the gate R close to the right-hand dot. We account for it by replacing the right-dot orbital energy $\varepsilon_R \rightarrow \varepsilon_R + V_0 \sin(2\pi ft)$, where V_0 and f are respectively the modulation amplitude and frequency. To make contact with earlier studies on electronic double-dots [40–46], we start at zero magnetic field. Figure 2(a) shows the tunneling current as a function of the detuning $\Delta\varepsilon$ and microwave power for a high modulation frequency $f = 15.9$ GHz. The set of interference fringes separated in detuning by $2\pi\hbar f$ corresponds precisely to the PAT pattern studied in electronic devices, with characteristic oscillations in intensity as a function of power. The pattern is reproduced theoretically in Fig. 2(b) by calculating the time-averaged current in the density-matrix rate equation approach [39, 50–52] applied to our four-level model. As the microwave frequency is reduced to 6.7 GHz, the PAT fringes are closer in detuning as seen in experiment, Fig. 2(c) and theory, Fig. 2(d). The interference fringes are broadened by decoherence [39] allowing us to extract the value of $T_2^* \approx 60$ and 75 ps for $f = 15.9$ GHz and 6.7 GHz, respectively. For an even lower frequency $f = 4$ GHz [Fig. 2(e) experiment and (f) theory] the fringes coalesce and form funnel-shaped features re-

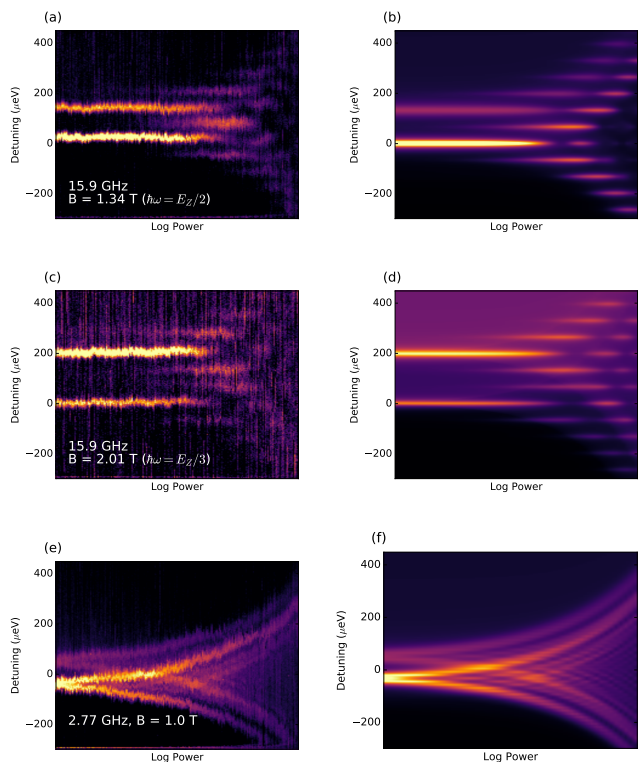


FIG. 3: LZSM interferometry of a single hole at a nonzero magnetic field. Tunneling current measured (a) and calculated (b) as a function of detuning and microwave power for the driving frequency $f = 15.9$ GHz and the magnetic field $B = 1.34$ T. The field is chosen so that the Zeeman energy $E_Z = 2\hbar f$. Panels (c) and (d) show the current at $B = 2$ T, i.e., $E_Z = 3\hbar f$, with the same microwave modulation. Panels (e) and (f) show respectively the tunneling current measured and calculated at $B = 1$ T for driving frequency $f = 2.77$ GHz.

lated to the LZSM spectra recorded in electronic systems modulated by single pulses [53–56]. Here the extracted $T_2^* = 90$ ps, the apparent systematic increase being due most likely to decreased charge noise at lower microwave frequencies.

The LZSM spectra are dramatically different in a nonzero magnetic field. Figures 3(a) and (c) show respectively the tunneling current as a function of microwave power for high frequency modulation ($f = 15.9$ GHz) and two values of magnetic field, $B = 1.34$ T and $B = 2$ T, respectively. Figure 3(e) shows the current measured at $B = 1$ T and a low-frequency modulation ($f = 2.77$ GHz). Figures 3(b), (d), and (f) show the results of corresponding simulations. Here the spin-conserving and spin-flipping tunneling channels become nondegenerate resulting in the appearance of two sets of interference fringes. In Fig. 3(a) we are in the PAT regime. Here the magnetic field was chosen so that the resulting Zeeman energy $E_Z = 2\hbar f$, leading to the overlap of first-order interference features of the two patterns. An increase

of the magnetic field to 2 T gives the Zeeman energy $E_Z = 3hf$, resulting in a relative shift of these patterns in detuning, as seen in Fig. 3(c). In Fig. 3(e) we recover the characteristic low-frequency funnel-shaped fringes at the field of $B = 1$ T. The current maxima evolve from the two-peak structure at low power, through broader, but separate interference patterns at intermediate powers, towards a complex, overlapping structure at high powers. The LZSM driving introduces a precise timing metric, which allows to fit the tunneling elements t_N and t_F as well as the decoherence times T_{2N} and T_{2F} characterizing the spin-conserving and spin-flipping tunneling process, respectively [50]. We find nearly power-independent values of $t_N = 0.26 \pm 0.02 \mu\text{eV}$ and $t_F = 0.28 \pm 0.04 \mu\text{eV}$. Moreover, decoherence times $T_{2N} \approx T_{2F} = T_2^*$ appear to decrease from ~ 120 ps down to ~ 80 ps as the power increases, which is probably due to the heating of the sample. The simulation result in Fig. 3(d) shows the current calculated for a power-independent value of $T_2^* = 90$ ps in excellent agreement with experimental data. The existence of the LZSM interference pattern for both tunneling processes indicates that the spin-flipping channel is as strong and as coherent as the usual spin-conserving one. As a result, we deal with a hybrid spin-charge qubit spanned in the basis of four spin-orbital states, with the orthogonal degrees of freedom being the position and the spin of the hole. This system differs from the electronic singlet-triplet hybrid qubit demonstrated recently in silicon [57] in that here the tunneling of the hole from one dot to another can be realized both without and with spin flip, offering enhanced functionality and control.

The relative shift of the two LZSM patterns can be tuned with the magnetic field. To demonstrate this, in Fig. 4(a) we plot the PAT spectra at the microwave power of 5 dBm as a function of the magnetic field, while panel (b) shows the result of simulation. With an excellent agreement between the experiment and theory, we find two clear families of lines. The field-independent (horizontal) features correspond to the spin-conserving transitions, while the field-dependent traces denote the spin-flipping resonances. The second family consists of lines with positive and negative slopes, corresponding to the two spin-flip transitions possible when tunneling from the right to the left dot, i.e., $(0, \uparrow) \rightarrow (\downarrow, 0)$ and $(0, \downarrow) \rightarrow (\uparrow, 0)$.

Due to their different dependence on the magnetic field, the different families exhibit intersections (degeneracies) at critical values of the field and detuning. This is the central result of our LZSM interferometry study. In Fig. 4 we discuss the two possible types of these intersections. The first one, denoted in panel (b) as (1), involves two fringes, one positively and one negatively sloped in the magnetic field. The diagrammatic description of this condition is shown in panel (c). Since the positions of both fringes are field-dependent, they both correspond to spin-flipping tunneling, albeit at a differ-

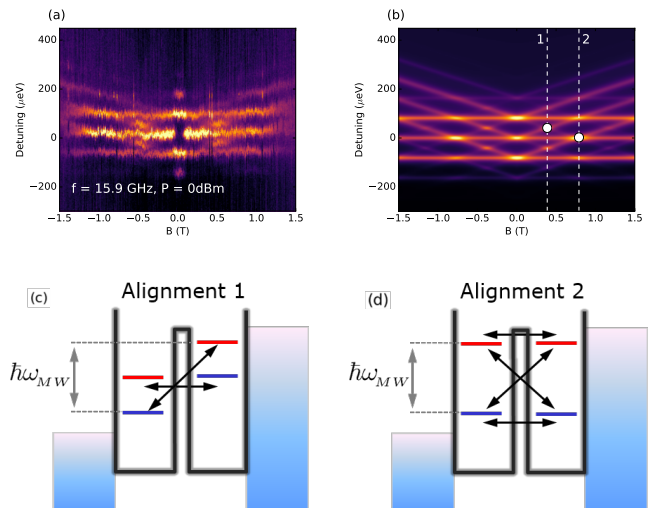


FIG. 4: (a), (b) Measured and calculated tunneling current as a function of detuning (vertical axis) and magnetic field (horizontal axis) at microwave frequency $f = 19.56$ GHz and power 0 dBm. Panels (c) and (d) show the alignment of quantum dot levels and the resulting tunneling pathways respectively at conditions (1) and (2) from panel (b).

ent PAT order (here, $n = 0$ and $n = +1$). The condition for its occurrence connects the detuning, the Zeeman energy, and the microwave frequency as $\Delta\varepsilon = E_Z = \pi\hbar f$. Here, the two resonant tunneling channels are enabled simultaneously, but remain independent, and the resultant tunneling current is a simple sum of the two contributions. This is why in Fig. 4(a) and (b) we see a clear enhancement (a bright spot) compared to the visibility of the linear features leading into it.

The independence of the two channels makes it possible to invert the arbitrary hole spin state in tunneling from the right to the left dot. Indeed, let us prepare the right-dot hole state in the form $\alpha|(0, \uparrow)\rangle + \beta|(0, \downarrow)\rangle$. At this resonance point, the state is transferred (within the LZSM process) to the left-dot state $\beta|(\uparrow, 0)\rangle + \alpha e^{i\phi}|(\downarrow, 0)\rangle$, with a possible phase factor ϕ dependent on the relative phase of the spin-flipping and spin-conserving processes. This enables a complete, electrically-controlled hole spin flip, while the control over the phase can be achieved e.g. through engineering of the Rashba SOI. In our LZSM study we apply a monochromatic microwave modulation, causing the hole to tunnel back and forth between the dots. However, the hole could be transferred to the left dot by employing appropriate pulse shaping techniques.

The second type of intersections is denoted by the condition (2) in Fig. 4(b), and is visualized schematically in panel (d). At such three-fold intersections, spin-flipping and spin-conserving channels of different interference orders are simultaneously active. In this case, $\Delta\varepsilon = 0$ and $E_Z = 2\pi\hbar f$, resulting in coincidence of $n = \pm 1$ spin-flipping and $n = 0$ spin-conserving processes. The

three channels depicted in the diagram (d) share common spinors, i.e., the process can be seen as a closed loop, evident from the alignment of arrows in the diagram. This opens a possibility of quantum interference, whereby the tunneling current could be suppressed completely, even though the energy matching conditions are met, in analogy to the coherent population trapping process. Theory predicts that the required balance of effective tunneling matrix elements could be achieved by an appropriate choice of the microwave power [50]. We note that a demonstration of such interference would be challenging in an electron system due to the disparity of the spin-conserving and spin-flipping elements.

In summary, we have applied the LZSM interferometry to study the coherent tunneling of a single hole between the dots of a gated lateral double-dot device. In a transport experiment at zero magnetic field we reproduced in all detail the interference patterns known from the electronic systems, both at high and low driving frequencies. At finite fields we demonstrated the coexistence of two, equally strong and equally coherent tunneling channels - one spin-conserving and one spin-flipping, the latter enabled by the strong SOI in our system. The resulting formation and coincidence of different photon-assisted tunneling pathways was studied in high-driving frequency LZSM interferometry. One such coincidence enables a complete inversion (flip) of an arbitrary spin state of the hole as it tunnels between the dots. At the other complex resonance point the hole visits the spin up and down orbitals of the left and right dots in a closed loop. Such a closed transport pathway is a prerequisite for single-hole quantum interference phenomena in analogy with the Aharonov-Bohm effect.

Acknowledgment. AB and SS thanks the Natural Sciences and Engineering Research Council of Canada for financial support. This work was performed in part at the Center for Integrated Nanotechnologies, a U.S. DOE, Office of Basic Energy Sciences user facility, and Sandia National Laboratories, a multi-mission laboratory managed and operated by National Technology and Engineering Solutions of Sandia, LLC., a wholly owned subsidiary of Honeywell International, Inc., for the U.S. Department of Energy's National Nuclear Security Administration under contract DE-NA-0003525.

* Corresponding author, email: sergei.studenikin@nrc.ca

† Corresponding author, email: andy.sachrajda@nrc.ca

- [1] M. A. Nielsen and I. L. Chuang, *Quantum Computation and Quantum Information*, Cambridge University Press, Cambridge, UK, 2010.
- [2] *Semiconductor Quantum Bits*, F. Henneberger and O. Benson (Eds.), Pan Stanford Publishing, Singapore, 2009.
- [3] J. Yoneda, T. Otsuka, T. Takakura, M. Pioro-Ladriere, R. Brunner, H. Lu, T. Nakajima, T. Obata, A. Noiri, C. J. Palmstroem, Ac C. Gossard, and S. Tarucha, *Appl. Phys. Express* **8**, 084401 (2015).
- [4] E. A. Laird, C. Barthel, E. I. Rashba, C. M. Marcus, M. P. Hanson, and A. C. Gossard, *Semicond. Sci. Technol.* **24**, 064004 (2009).
- [5] F. Forster, M. Muhlbacher, D. Schuh, W. Wegscheider, and S. Ludwig, *Phys. Rev. B* **91**, 195417 (2015).
- [6] F. H. L. Koppens, C. Buizert, K. J. Tielrooij, I. T. Vink, K. C. Nowack, T. Meunier, L. P. Kouwenhoven, and L. M. K. Vandersypen, *Nature* **442**, 766 (2006).
- [7] F. H. L. Koppens, K. C. Nowack, and L. M. K. Vandersypen, *Phys. Rev. Lett.* **100**, 236802 (2008).
- [8] M. Veldhorst, J. C. C. Hwang, C. H. Yang, A. W. Leenstra, B. de Ronde, J. P. Dehollain, J. T. Muhonen, F. E. Hudson, K. M. Itoh, A. Morello, and A. S. Dzurak, *Nature Nanotechnol.* **9**, 981 (2014).
- [9] S. Datta and B. Das, *Appl. Phys. Lett.* **56**, 665 (1990).
- [10] L. R. Schreiber, F. R. Braakman, T. Meunier, V. Calado, J. Danon, J. M. Taylor, W. Wegscheider, and L. M. K. Vandersypen, *Nature Comm.* **2**, 556 (2011).
- [11] K. C. Nowack, F. H. L. Koppens, Yu. V. Nazarov, and L. M. K. Vandersypen, *Science* **318**, 1430 (2007).
- [12] S. Nadj-Perge, S. M. Frolov, E. P. A. M. Bakkers, and L. P. Kouwenhoven, *Nature* **468**, 1084 (2010).
- [13] A. Pfund, I. Shorubalko, K. Ensslin, and R. Leturcq, *Phys. Rev. B* **76**, 161308(R) (2007).
- [14] J. M. Nichol, S. P. Harvey, M. D. Shulman, A. Pal, V. Umansky, E. I. Rashba, B. I. Halperin, and A. Yacoby, *Nature Comm.* **6**, 7682 (2015).
- [15] S. Nadj-Perge, S. M. Frolov, J. W. W. van Tilburg, J. Danon, Yu. V. Nazarov, R. Algra, E. P. A. M. Bakkers, and L. P. Kouwenhoven, *Phys. Rev. B* **81**, 201305(R) (2010).
- [16] T. Fujita, P. Stano, G. Allison, K. Morimoto, Y. Sato, M. Larsson, J.-H. Park, A. Ludwig, A. D. Wieck, A. Oiwai, and S. Tarucha, *Phys. Rev. Lett.* **117**, 206802 (2016).
- [17] V. F. Maisi, A. Hofmann, M. Roosli, J. Basset, C. Reichl, W. Wegscheider, T. Ihn, and K. Ensslin, *Phys. Rev. Lett.* **116**, 136803 (2016).
- [18] P. Szumniak, S. Bednarek, B. Partoens, and F. M. Peeters, *Phys. Rev. Lett.* **109**, 107201 (2012).
- [19] P. Szumniak, S. Bednarek, J. Pawlowski, and B. Partoens, *Phys. Rev. B* **87**, 195307 (2013).
- [20] X. J. Wang, S. Chesi, and W. A. Coish, *Phys. Rev. Lett.* **109**, 237601 (2012).
- [21] Jan Fischer, W. A. Coish, D. V. Bulaev, and D. Loss, *Phys. Rev. B* **78**, 155329 (2008).
- [22] G. Burkard, *Nature Mater.* **7**, 100 (2008).
- [23] J. Fisher and D. Loss, *Phys. Rev. Lett.* **105**, 266603 (2010).
- [24] A. Tartakovskii, *Nature Photon.* **5**, 647 (2011).
- [25] D. Heiss, S. Schaeck, H. Huebl, M. Bichler, G. Abstreiter, J. J. Finley, D. V. Bulaev, and D. Loss, *Phys. Rev. B* **76**, 241306(R) (2007).
- [26] B. D. Gerardot, D. Brunner, P.A. Dalgarno, P. Ohberg, S. Seidl, M. Kroner, K. Karrai, N. G. Stoltz, P. M. Petroff, and R. J. Warburton, *Nature (London)* **451**, 441 (2008).
- [27] D. Brunner, B.D. Gerardot, P. A. Dalgarno, G. Wust, K. Karrai, N. G. Stoltz, P. M. Petroff, and R. J. Warburton, *Science* **325**, 70 (2009).
- [28] F. Fras, B. Eble, B. Siarry, F. Bernardot, A. Miard, A. Lemaitre, C. Testelin, and M. Chamorro, *Phys. Rev. B*

- 86**, 161303(R) (2012).
- [29] S. Varwig, A. Rene, A. Greilich, D. R. Yakovlev, D. Reuter, A. D. Wieck, and M. Bayer, *Phys. Rev. B* **87**, 115307 (2013).
- [30] K. De Greve, P. L. McMahon, D. Press, T. D. Ladd, Dirk Bisping, C. Schneider, M. Kamp, L. Worschech, S. Hoffing, A. Forchel, and Y. Yamamoto, *Nature Phys.* **7**, 872 (2011).
- [31] R. Li, F. E. Hudson, A. S. Dzurak, and A. R. Hamilton, *Nano Lett.* **15**, 7314 (2015).
- [32] H. Bohuslavskiy, D. Kotekar-Patil, R. Maurand, A. Corna, S. Barraud, L. Bourdet, L. Hutin, Y.-M. Niquet, X. Jehl, S. De Franceschi, M. Vinet, and M. Sanquer, *Appl. Phys. Lett.* **109**, 193101 (2016).
- [33] F. A. Zwanenburg, C. E. W. M. van Rijmenam, Y. Fang, C. M. Lieber, and L. P. Kouwenhoven, *Nano Lett.* **9**, 1071 (2009).
- [34] A. P. Higginbotham, T. W. Larsen, J. Yao, H. Yan, C. M. Lieber, C. M. Marcus, and F. Kuemmeth, *Nano Lett.* **14**, 3582 (2014).
- [35] B. Voisin, R. Maurand, S. Barraud, M. Vinet, X. Jehl, M. Sanquer, J. Renard, and S. De Franceschi, *Nano Lett.* **16**, 88 (2016).
- [36] R. Maurand, X. Jehl, D. Kotekar-Patil, A. Corna, H. Bohuslavskiy, R. Lavieville, L. Hutin, S. Barraud, M. Vinet, M. Sanquer, and S. De Franceschi, *Nature Comm.* **7**, 13575 (2016).
- [37] D. Q. Wang, O. Klochan, J.-T. Hung, D. Culcer, I. Farrer, D. A. Ritchie, and A. R. Hamilton, *Nano Lett.* **16**, 7685 (2016).
- [38] A. Bogan, S. A. Studenikin, M. Korkusinski, G. C. Aers, L. Gaudreau, P. Zawadzki, A. S. Sachrajda, L. A. Tracy, J. L. Reno, and T. W. Hargett, *Phys. Rev. Lett.* **118**, 167701 (2017).
- [39] S. N. Shevchenko, S. Ashhab, and F. Nori, *Phys. Reports* **492**, 1 (2010).
- [40] T. H. Oosterkamp, T. Fujisawa, W. G. van der Wiel, K. Ishibashi, R. V. Hijman, S. Tarucha, and L. P. Kouwenhoven, *Nature* **395**, 873 (1998).
- [41] L. R. Schreiber, F. R. Braakman, T. Meunier, V. Calado, J. Danon, J. M. Taylor, W. Wegscheider, and L. M. K. Vandersypen, *Nature Commun.* **2**, 556 (2011).
- [42] M. F. Gonzalez-Zalba, S. N. Shevchenko, S. Barraud, J. R. Johansson, A. J. Ferguson, F. Nori, and A. C. Betz, *Nano Lett.* **16**, 1614 (2016).
- [43] J. Stehlik, Y. Dovzhenko, J. R. Petta, J. R. Johansson, F. Nori, H. Lu, and A. C. Gossard, *Phys. Rev. B* **86**, 121303(R) (2012).
- [44] F. Forster, G. Petersen, S. Manus, P. Hanggi, D. Schuh, W. Wegscheider, S. Kohler, and S. Ludwig, *Phys. Rev. Lett.* **112**, 116803 (2014).
- [45] J. R. Petta, A. C. Johnson, C. M. Marcus, M. P. Hanson, and A. C. Gossard, *Phys. Rev. Lett.* **93**, 186802 (2004).
- [46] F. R. Braakman, J. Danon, L. R. Schreiber, W. Wegscheider, and L. M. K. Vandersypen, *Phys. Rev. B* **89**, 075417 (2014).
- [47] L. A. Tracy, T. W. Hargett, and J. L. Reno, *Appl. Phys. Lett.* **104**, 123101 (2014).
- [48] D. Bulaev and D. Loss, *Phys. Rev. Lett.* **98**, 097202 (2007).
- [49] D. Bulaev and D. Loss, *Phys. Rev. Lett.* **95**, 076805 (2005).
- [50] Supplementary material accompanying this paper.
- [51] G. Platero and R. Aguado, *Phys. Reports* **395**, 1 (2004).
- [52] J. Villavicencio, I. Maldonado, E. Cota, and G. Platero, *Phys. Rev. B* **88**, 245305 (2013).
- [53] J. R. Petta, H. Lu, and A. C. Gossard, *Science* **327**, 669 (2007).
- [54] S. A. Studenikin, G. C. Aers, G. Granger, L. Gaudreau, A. Kam, P. Zawadzki, Z. R. Wasilewski, and A. S. Sachrajda, *Phys. Rev. Lett.* **108**, 226802 (2012).
- [55] G. Poulin-Lamarre, J. Thorgrimson, S. A. Studenikin, G. C. Aers, A. Kam, P. Zawadzki, Z. R. Wasilewski, and A. S. Sachrajda, *Phys. Rev. B* **91**, 125417 (2015).
- [56] M. Korkusinski, S. A. Studenikin, G. Aers, G. Granger, A. Kam, and A. S. Sachrajda, *Phys. Rev. Lett.* **118**, 067701 (2017).
- [57] Z. Shi, C. B. Simmons, J. R. Prance, J. K. Gamble, T. S. Koh, Y.-P. Shim, X. Hu, D. E. Savage, M. G. Lagally, M. A. Eriksson, M. Friesen, and S. N. Coppersmith, *Phys. Rev. Lett.* **108**, 140503 (2012).

Supplementary material for Landau-Zener-Stückelberg-Majorana interferometry of a single hole

SAMPLE FABRICATION

The experimental study was performed on a double quantum dot (DQD) fabricated from an undoped GaAs/Al_xGa_{1-x}As ($x=50\%$) heterostructure (VA0670) employing lateral split-gate technology [S1–S4]. A suitable DQD potential profile was defined by the deposited lateral Ti/Au gates. A scanning electron micrograph (SEM) of the gate layout is shown in Fig. 1(a) of the main text. Holes were generated by a global gate deposited above the structure (not shown in Fig. 1(a) of the main text) separated by a 110 nm-thick Al₂O₃ dielectric layer grown by an atomic layer deposition technique. Left and right plunger gates, labeled as L and R, respectively, were used to tune individually the hole potentials in each dot, while the central gate C was used to adjust the interdot tunneling barrier. The sample was cooled down in a dilution refrigerator at the nominal electron temperature ~ 100 mK. For transport measurements a DC voltage ~ 2 mV was applied to the right Ohmic contact and DC current through the dot was measured using a DL Instruments model 1211 current preamplifier connected to the left Ohmic contact.

THEORETICAL MODEL

The hole manifold with Bloch angular momentum $J = 3/2$ is composed of two HH states, with $J_z = \pm 3/2$, and two LH states, with $J_z = \pm 1/2$. This manifold is described by the Luttinger-Kohn Hamiltonian, which provides the HH (LH) single-band energy in the anisotropic form $\hat{T}_{HH(LH)} = (\gamma_1 \pm \gamma_2)(p_x^2 + p_y^2)/2m_0 + (\gamma_1 \mp 2\gamma_2)p_z^2/2m_0 + U(x, y) + V_H(z)$. Here \vec{p} is the momentum operator, m_0 is the free electron mass, $U(x, y)$ is the lateral confinement generated by gates, and $V_H(z)$ is the vertical confinement produced by the heterointerface and the top accumulation gate. The anisotropic effective masses are defined by the Luttinger parameters (for GaAs, $\gamma_1 = 6.95$ and $\gamma_2 = 2.25$) producing the hole subband masses $m_{HH}(z) = 0.41m_0$ and $m_{LH}(z) = 0.09m_0$. As a consequence, the tight vertical confinement $V_H(z)$ results in a splitting of the hole subbands, with the lowest-lying HH subband lying lower in energy than the lowest-lying LH subband. This splitting is large enough to justify the further development of our model in the basis of HH states only, with the influence of LH subbands included perturbatively [S4]. Following Bulaev and Loss [S5] we write the perturbative Hamiltonian for a single confined HH as

$$\hat{H} = \frac{1}{2m}(p_x^2 + p_y^2) + U(x, y) + \frac{1}{2}g^*\mu_B B_z \sigma_z + H_{SO}, \quad (\text{S1})$$

with the effective spin-orbit (SO) interaction

$$H_{SO} = i\alpha E_{\perp}(\sigma_+ p_-^3 - \sigma_- p_+^3) + \beta(\sigma_+ p_- p_+ p_- - \sigma_- p_+ p_- p_+).$$

Here, the in-plane momentum operator $\vec{p} = -i\hbar\nabla + \frac{e}{c}\vec{A}$ contains the magnetic-field dependent term with e being the hole charge, c the speed of light, and \vec{A} the magnetic vector potential, such that the field $\vec{B} = \nabla \times \vec{A}$. In the following we assume $\vec{B} = [0, 0, B_z]$ to be perpendicular to the heterointerface, which results in the Zeeman term (the third term in the above Hamiltonian) scaled by the effective hole g-factor g^* , with μ_B being the Bohr magneton. We also introduce the effective two-level spin operator σ_z such that $J_z = \frac{3}{2}\sigma_z$ [S5]. The two other (in-plane) components of that operator define the spin raising (lowering) operator $\sigma_{\pm} = (\sigma_x \pm i\sigma_y)/2$ appearing in H_{SO} together with $p_{\pm} = p_x \pm ip_y$. The SO Hamiltonian accounts for Rashba and Dresselhaus interactions characterized respectively by parameters α and β [S6–S8]. The Rashba term is additionally scaled by the effective electric field E_{\perp} produced by the accumulation gate.

As evident from the Hamiltonian (S1), the SO interaction couples the hole spin and orbital degrees of freedom, which leads to the rotation of the hole spin as it tunnels through the device. This tunneling channel appears in addition to the usual, spin-conserving channel, involving the simple tunneling of the hole across the interdot potential barrier created electrostatically by the gates (this barrier is a component of the lateral confinement $U(x, y)$). To bring out these two effects clearly, and to enable quantitative fitting to experimental data, we now map the Hamiltonian (S1) onto a two-site Hubbard model along the procedure described in Ref. [S9]. To this end, we choose the basis in the form of four spin-orbitals (spinors) $\{|L, \uparrow\rangle, |L, \downarrow\rangle, |R, \uparrow\rangle, |R, \downarrow\rangle\}$, where L (R) labels the orbital part being centered on the left (right) dot, while the arrow denotes the hole spin. We do not specify the explicit functional form of these spinors, but choose them to be orthogonal, which eliminates the need of accounting for the overlap matrix. We can now generate

the matrix elements of our Hamiltonian against this localized basis. The diagonal elements, i.e., the energies of each basis state, attain the form $\langle L, \uparrow | H | L, \uparrow \rangle = \varepsilon_L + \frac{1}{2}E_Z$, and analogously for the three other spinors. The onsite energy ε_L is a free parameter, tunable by gate voltages. The analogous parameter for the right-hand dot orbitals is denoted as ε_R . The spin-conserving tunneling process is enabled by the matrix element $\langle L, \uparrow | H | R, \uparrow \rangle = \langle L, \downarrow | H | R, \downarrow \rangle = -t_N$. Because of the conservation of spin, this element is computed without any contribution of H_{SO} , and therefore has the same meaning as that used to describe lateral gated electron systems [S9]. The spin-flipping process, on the other hand, is quantified by $\langle L, \uparrow | H | R, \downarrow \rangle = -i|t_F|e^{-i\phi}$. Owing to the form of H_{SO} , this element is a complex number, with the magnitude $|t_F|$ and phase ϕ , the latter dependent on the relative strength of the Rashba and Dresselhaus SO terms. We have found that the theoretical results in this work are insensitive to the exact value of ϕ and in the following we choose $\phi = 0$ for simplicity.

As a result of the mapping, we end up with the Hubbard Hamiltonian

$$\hat{H} = \begin{bmatrix} \varepsilon_L + E_Z/2 & 0 & -t_N & -it_F \\ 0 & \varepsilon_L - E_Z/2 & -it_F & -t_N \\ -t_N & it_F & \varepsilon_R + E_Z/2 & 0 \\ it_F & -t_N & 0 & \varepsilon_R - E_Z/2 \end{bmatrix}. \quad (\text{S2})$$

identical to the form shown in the main text. The values of the parameters t_N and t_F and the hole g-factor g^* are obtained by fitting to the experimental data.

THEORETICAL SIMULATIONS OF THE EXPERIMENTAL SYSTEM

Coherent and incoherent processes in single-hole tunneling

As described in the main text, we study the coherent dynamics of our system in magneto-transport spectroscopy by measuring the tunneling current as a function of the detuning $\Delta\varepsilon = \varepsilon_R - \varepsilon_L$ and the magnetic field. The sinusoidal microwave modulation for the Landau-Zener-Stückelberg-Majorana interferometry is applied to the gate located close to the right-hand dot. We account for it by replacing $\varepsilon_R \rightarrow \varepsilon_R + V_0 \sin(2\pi ft)$, where V_0 and f are respectively modulation amplitude and frequency.

Figure S1(a) shows schematically the alignment of levels at $\Delta\varepsilon < 0$. The hole tunnels from the right lead and into the left lead with spin-independent tunneling rates Γ_R and Γ_L , respectively. The rates are chosen to be high, so that the tunneling current is determined by the transparency of the interdot barrier. Due to the large source-drain voltage $\Delta V_{SD} = 2$ mV, both right-dot spinors are populated equally. Without microwave modulation, in the alignment shown in Fig. S1(a) the current is blocked, since the hole is trapped on the state $|R \downarrow\rangle$ (blue arrow). Current maxima are expected at detunings $\Delta\varepsilon = 0$ (Fig. S1(b)) and $\Delta\varepsilon = E_Z$ (Fig. S1(d)) corresponding to the spin-conserving and spin-flipping tunneling, respectively. The decoherence of these processes is characterized by times T_{2N} and T_{2F} , respectively (not shown in diagrams). At intermediate ($0 < \Delta\varepsilon < E_Z$, Fig. S1(c)) and large detunings ($\Delta\varepsilon > E_Z$, Fig. S1(e)) transport can occur only by incoherent phonon-assisted leakage processes, described by charge relaxation times T_{1N} for the spin-conserving channel (black arrows), and T_{1F} for the spin-flipping channel (green arrows). Depending on the detuning, these processes can partially cancel out (panel (c)) or add up (panel (e)) producing different net leakage current. The third type of relaxation process involves the spin flip within one dot, and is characterized by the time T_{1S} shown schematically by the vertical arrows in Fig. S1(d).

Density-matrix approach

In our theoretical model we account for all coherent and incoherent processes in the density-matrix rate equation approach [S10–S12], in which we calculate the time-averaged current as a function of the detuning, magnetic field, and microwave power. The quantum master equation for the density matrix $\varrho(t)$ has the form

$$\frac{d}{dt}\varrho(t) = -\frac{i}{\hbar}[H, \varrho(t)] + \Gamma_{in}\varrho(t) + \Gamma_{out}\varrho(t) + \Gamma_{T2}\varrho(t) + \Gamma_{T1}\varrho(t) + \Gamma_{T1S}\varrho(t). \quad (\text{S3})$$

The density matrix

$$\rho(t) = \sum_{i,j=1}^4 \rho_{ij}|i\rangle\langle j| \quad (\text{S4})$$

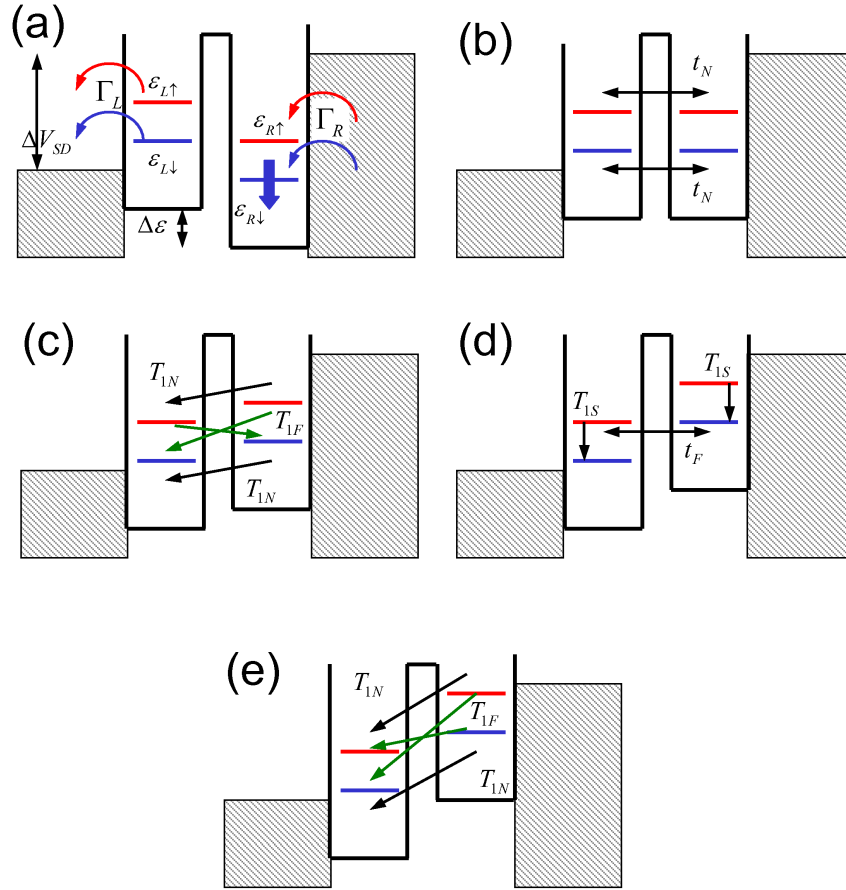


FIG. S1: Schematic energy diagrams at large source-drain voltage V_{SD} and with different detunings $\Delta\varepsilon < 0$ (a), $\Delta\varepsilon = 0$ (b), $0 < \Delta\varepsilon < E_Z$ (c), $\Delta\varepsilon = E_Z$ (d), and $\Delta\varepsilon > E_Z$ (e). Double arrows denote resonant tunneling processes, while single arrows denote leakage channels, spin-conserving (black) and spin-flipping (green).

is defined in the same four-spinor basis as the Hamiltonian (S2). In the master equation the first term on the right-hand side describes the coherent time evolution of the system (i.e., tunneling). The other terms describe the tunneling of a single hole from the right-hand lead into the right-hand dot (the second term), into the left-hand lead from the left-hand dot (the third term), the decoherence process (the fourth term), and the T_1 -type relaxation processes (the fifth and sixth term).

In modeling the tunnel coupling to the leads we follow the Born-Markov secular approximation described, e.g., in Refs. S13, S14. As already mentioned, owing to the large source-drain bias we assume that the tunneling rates of both hole spin species are equal and characterized by the rates Γ_R for the right-hand lead and Γ_L for the left-hand lead. Modeling of the filling of the right-hand dot involves modifying the appropriate diagonal density matrix elements subject to the condition that the total population of the double dot must not exceed one hole. On the other hand, the emptying of the left-hand dot is modeled by modifying both diagonal and offdiagonal elements, i.e., we account for contributions to both incoherent exponential population decay and decoherence processes.

The decoherence processes are modeled by suppressing the offdiagonal density matrix elements connecting single-hole configurations which in the Hamiltonian (S2) are linked by a coherent tunneling element t_N or t_F . For example, for the spin-flip tunneling process we have $\langle L, \downarrow | \Gamma_{T2} \rho(t) | R, \uparrow \rangle = -\langle L, \downarrow | \rho(t) | R, \uparrow \rangle / T_{2F}$, and for the non-spin-flip process $\langle L, \downarrow | \Gamma_{T2} \rho(t) | R, \downarrow \rangle = -\langle L, \downarrow | \rho(t) | R, \downarrow \rangle / T_{2N}$.

The T_1 -type relaxation processes are modeled in a fashion similar to the incoherent coupling to the leads, i.e., one state, e.g., $|R, \uparrow\rangle$, is depopulated at a constant rate $1/T_{1F}$ while another, e.g., $|L, \downarrow\rangle$ is populated at the same rate, obeying the overall charge conservation rule. The depopulation of the “source” level also contributes to all decoherence processes involving that level. This example describes the incoherent spin-flip leakage through the barrier, but, as

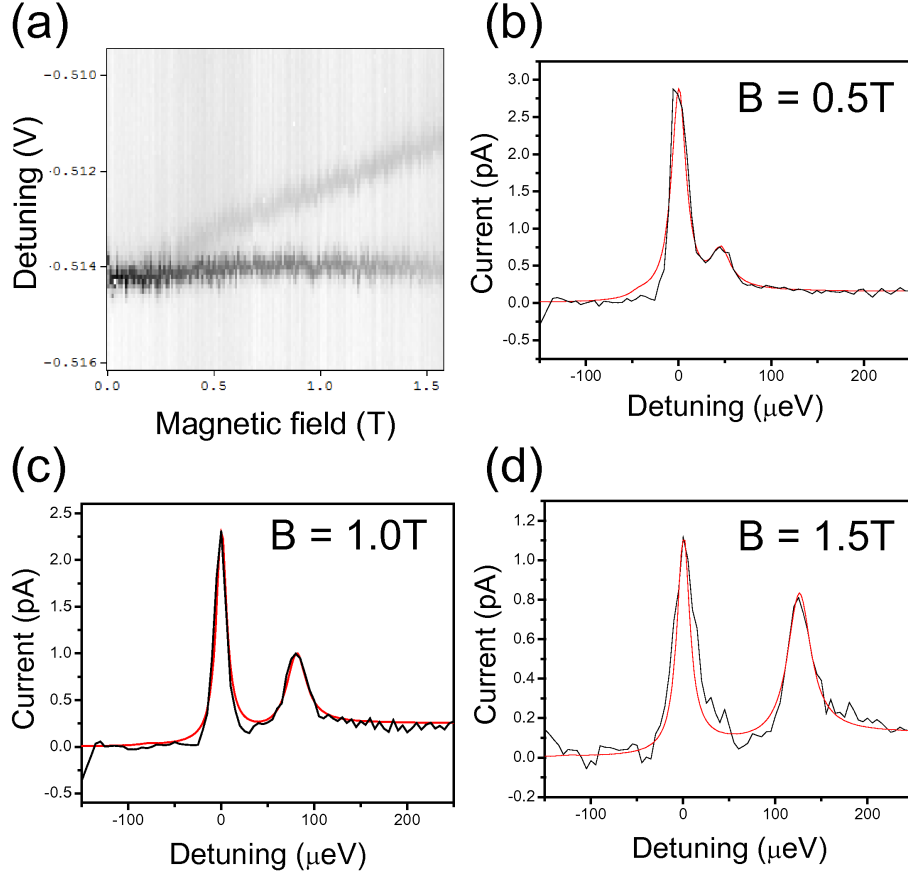


FIG. S2: (a) Tunneling current measured as a function of the voltage on gate R (vertical axis) and magnetic field (horizontal axis). Panels (b), (c), and (d) show the current as a function of detuning at $B = 0.5\text{ T}$, 1 T , and 1.5 T , measured (black line) and fitted theoretically (red line).

depicted in Figs. S1(c) and (e), we also account for the spin-conserving leakage characterized by the time T_{1N} . Finally, as shown in Fig. S1(d), we also account for the spin-flip relaxation process characterized by the time T_{1S} . The orbitals connected by this process belong to the same quantum dot.

We integrate the master equation numerically using the four-point Runge-Kutta approach. This allows us to compute the complete density matrix $\varrho(t)$ at any moment t . The average current integrated over the total time of $T_{total} = 5\ \mu\text{s}$ is expressed as

$$\bar{I} = \frac{e\Gamma_L}{T_{total}} \int_0^{T_{total}} dt [\varrho(1,1)(t) + \varrho(2,2)(t)], \quad (\text{S5})$$

i.e., an integral over the time-dependent populations of levels $|L, \uparrow\rangle$ and $|L, \downarrow\rangle$.

Fitting to experimental magnetotransport spectra

To quantify our theoretical model, we map out the tunneling current as a function of the static detuning $\Delta\varepsilon$ and the magnetic field in the magnetotransport experiment. The map, shown in Fig. S2(a), reveals two resonant features. The detuning corresponding to one of them is approximately independent of the field, while the detuning corresponding to the other one increases linearly with the field. Based on our model, we identify the first resonance as the spin-conserving resonant tunneling (at $\Delta\varepsilon = 0$, Fig. S1(b)), and the second one as the spin-flipping tunneling (at $\Delta\varepsilon = E_Z$, Fig. S1(d)). Figures S2(b), (c), and (d) show the current extracted from the panel (a) as a function of the detuning (rescaled by the lever arm of $50\ \mu\text{eV}/\text{mV}$) at $B = 0.5\text{ T}$, 1 T , and 1.5 T , respectively (black lines).

We extract all model parameters by producing the theoretical fits (red lines). By fitting the magnitude and width of the current maxima, corresponding to the resonant processes, we extract simultaneously the tunneling elements t_N and t_F , the tunneling rates from/to leads $\Gamma_L = \Gamma_R = 2$ GHz, the decoherence times $T_{2N} \approx T_{2F} = 80$ ps, the spin-flip relaxation time $T_{1S} = 0.75$ μ s, and the g-factor $g^* = 1.35$. The value of T_{1S} is consistent with the estimates obtained for a double-dot device in a many-hole regime [S15]. The value of g^* is similar to our previous result for the two-hole system [S4]. Finally, the leakage times $T_{1N} = 2.7$ μ s and $T_{1F} = 2.4$ μ s are extracted from the low-current regions at intermediate (Fig. S1(c)) and large detunings (Fig. S1(e)). The values of t_N and t_F obtained in this procedure are plotted as a function of the magnetic field in Fig. 1(f) of the main text (red and black dots, respectively).

Dependence of tunneling elements on the magnetic field

Based on the form of the Hamiltonian (S1) we can predict the trends of the dependence of both tunneling matrix elements t_N and t_F on the magnetic field. To this end, we define the orbitals centered on the left and right dot in the model Gaussian form: $\langle r|L\rangle = \frac{\sqrt{2}}{l\sqrt{\pi}} \exp\left(-\frac{(x+d)^2+y^2}{l^2}\right)$ and $\langle r|R\rangle = \frac{\sqrt{2}}{l\sqrt{\pi}} \exp\left(-\frac{(x-d)^2+y^2}{l^2}\right)$. With this choice the dots lie on the x axis and their centers are separated by the distance $2d$. The Gaussian form of the single-particle wave function corresponds to that of the lowest-energy state of the two-dimensional harmonic oscillator [S16]. Here l is the characteristic length defining the lateral extent of the orbitals. In the presence of the perpendicular magnetic field, $\frac{1}{l^2} = \frac{m}{\hbar} \sqrt{\omega_0^2 + \frac{1}{4}\omega_c^2}$, where m is the in-plane effective hole mass, $\hbar\omega_0$ is the characteristic frequency of our model harmonic confinement, and $\omega_c = \frac{eB}{mc}$ is the cyclotron frequency. As we can see, with the increase of the magnetic field the characteristic length l decreases, i.e., our localized orbitals contract. The last step in the preparation of our basis is the orthogonalization of the single-dot orbitals. We achieve this to first order in the Loewdin procedure by redefining our basis orbitals as $|\bar{L}\rangle = |L\rangle - \frac{1}{2}S|R\rangle$ and $|\bar{R}\rangle = |R\rangle - \frac{1}{2}S|L\rangle$ with $S = \exp\left(-2\frac{d^2}{l^2}\right)$ being the overlap of the original orbitals.

We now proceed to investigating the trends expected for the elements t_N and t_F . For the former, we assume the interdot barrier to be in the Gaussian form, $V(x) = V_0 \exp\left(-\frac{x^2}{b^2}\right)$ with V_0 being the potential height and b describing the spatial extent of the barrier along the x axis. We obtain

$$t_N = \langle \bar{L}|V(x)|\bar{R}\rangle = V_0 \exp\left(-2\frac{d^2}{l^2}\right) \sqrt{\frac{2b^2}{l^2 + 2b^2}} \left(1 - \exp\left(-2\frac{d^2}{2b^2 + l^2}\right)\right). \quad (\text{S6})$$

Following Ref. [S4], we take the model values of parameters $\hbar\omega_0 = 0.29$ meV, $m = 0.11m_0$, $d = 57.75$ nm. The best fit (red dashed line) to the experimental data (red symbols) plotted in Fig. 1(f) of the main text is obtained by using the model barrier with $b = 0.5d$ and $V_0 = 5$ meV. Since our model treatment does not account for the microscopic detail of the lateral confinement, such as the anisotropy of the individual dot potentials and the exact shape of the tunneling barrier, we do not expect an exact fit. However, our estimate agrees with the experiment in predicting the monotonic decrease of t_N as the magnetic field grows, due mainly to the decrease of the overlap between the orbitals (the first exponential factor in the above formula).

Let us now move on to the calculation of the element t_F . As is evident from the form of H_{SO} , here we need to compute an integral of generalized momentum in the third power against our model orbitals. We choose the magnetic vector potential in the form $\vec{A} = \frac{B}{2}[-y, x, 0]$ giving us the uniform magnetic field directed along the z axis. We note that, in principle, the localized orbitals $|L\rangle$ and $|R\rangle$ are defined with a local gauge, whose origin lies at coordinates $[-d, 0, 0]$ and $[+d, 0, 0]$, respectively. However, the Loewdin procedure mixes these two gauges, and for our model momentum we choose the global gauge with origin at $[0, 0, 0]$. To account for both Dresselhaus and Rashba terms we need to compute two momentum integrals, i.e., $\langle \bar{L}|p_- p_+ p_- |\bar{R}\rangle$ and $\langle \bar{L}|p_-^3 |\bar{R}\rangle$. As a result, we obtain the following complex matrix element:

$$\langle \bar{L} \uparrow | H_{SO} | \bar{R} \downarrow \rangle = -8\hbar^3 \alpha E_{\perp} \frac{d^3}{l^6} \exp\left(-2\frac{d^2}{l^2}\right) - i\beta\hbar^3 \left(\frac{8d}{l^4} - \frac{8d^3}{l^6} + \frac{d}{2l_B^4}\right) \exp\left(-2\frac{d^2}{l^2}\right), \quad (\text{S7})$$

with the magnetic length $l_B = \sqrt{\frac{\hbar}{m\omega_c}}$. In analogy to the element t_N , here we recover the exponential term related to the overlap of the two orbitals, indicating that the magnitude of t_F will decrease exponentially at large fields. However, unlike in t_N , the prefactors generated by the generalized momentum *increase* polynomially as the field grows. Thus, the resultant trend of the magnitude of t_F is the result of an interplay between the increasing magnitude of the

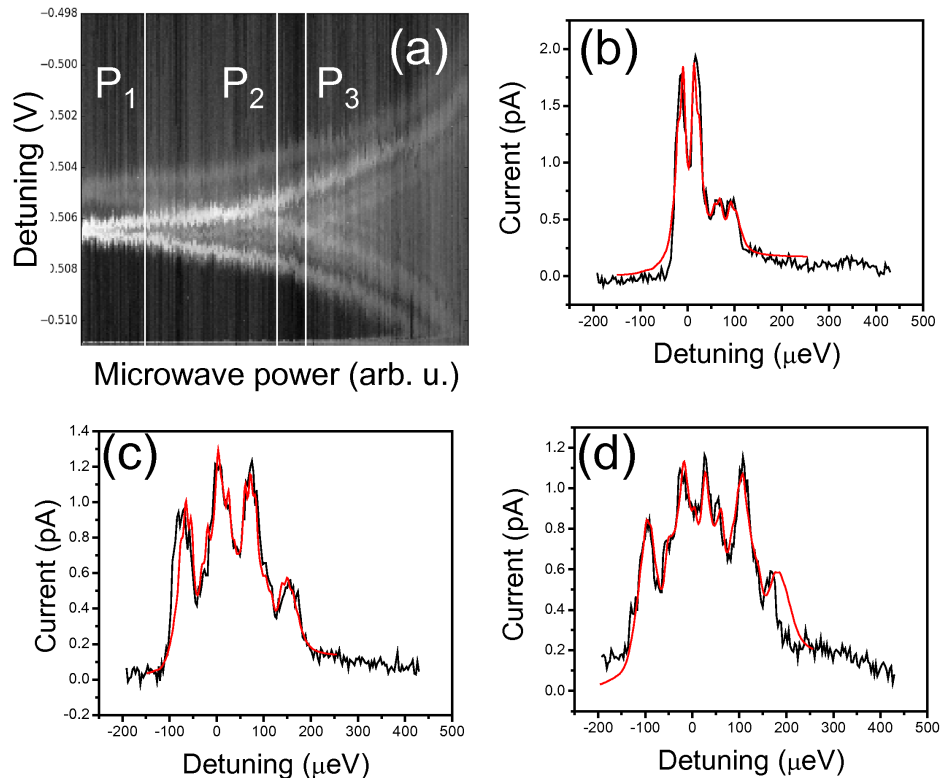


FIG. S3: (a) Tunneling current measured as a function of the voltage on gate R (vertical axis) and microwave power (horizontal axis, log scale) at the magnetic field $B = 1$ T. The microwave frequency $f = 2.77$ GHz. Panels (b), (c), and (d) show the current as a function of detuning at the three microwave powers, marked in the panel (a) as P_1 , P_2 , and P_3 , respectively. Black lines show the measured tunneling current, while red lines show the theoretical fit.

generalized momentum and the decreasing overlap between orbitals, producing an initial increase of t_F at small fields, followed by an exponential decrease for larger fields. This is exactly the trend predicted in Fig. 1(f) of the main text (black dashed line) and seen experimentally (black symbols). The fit of our model relationship to the experimental values was achieved by taking $\alpha E_{\perp} = \beta = 133.71$ meV.

QUANTITATIVE DESCRIPTION OF LZSM MAGNETO-TUNNELING SPECTRA

Figure S3(a) shows the tunneling current measured as a function of the microwave power at frequency $f = 2.77$ GHz and the magnetic field $B = 1$ T. This panel shows the unprocessed measurement results used to generate Fig. 3(e) of the main text. As discussed in the main text, the maxima evolve from the two-peak structure at low power, through broader, but separate interference patterns at intermediate powers, towards a complex, overlapping structure at high powers. In Fig. S3(b), (c), and (d) we compare the measured trace to the theoretical fit at powers denoted in panel (a) respectively by P_1 , P_2 , and P_3 . The LZSM driving introduces a precise timing metric, which allows to fit the tunneling elements t_N and t_F independently from the decoherence times T_{2N} and T_{2F} . The values of tunneling elements obtained in fitting are $t_N = 0.255$ μeV and $t_F = 0.205$ μeV for the power P_1 , $t_N = 0.26$ μeV and $t_F = 0.28$ μeV for the power P_2 , $t_N = 0.28$ μeV and $t_F = 0.31$ μeV for the power P_3 . The theoretical fits to the measured current are of high quality for all microwave modulation powers.

As shown in Figs. 2 and 3 of the main text, at high microwave frequencies f the interference pattern consists of a set of interference fringes separated in detuning by $2\pi\hbar f$. Only one set is observed at $B = 0$ (Fig. 2 of the main text), while at a nonzero field we see two sets, due to the spin-conserving and spin-flipping photon-assisted tunneling, respectively. Our theoretical fits, presented in the right-hand panels of Figs. 2 and 3 of the main text, were generated in the full density-matrix simulations. However, the large spacing between maxima allows to employ a perturbative regime, in which the power dependence of the peak amplitude of the n -th fringe is scaled by the Bessel function

$J_n(V_0/2\pi\hbar f)$ ($n = 0, \pm 1, \dots$), with V_0 being the microwave amplitude [S10]. These functions exhibit characteristic oscillations, with the central maximum ($n = 0$) being the only fringe visible at low powers. This dependence enables tuning of the effective tunneling elements with microwave power, and activate or deactivate the photon-assisted tunneling pathways, which are otherwise available based on matching of detuning, Zeeman energy, and the energy of the microwave photon.

* Corresponding author, email: sergei.studenikin@nrc.ca

† Corresponding author, email: andy.sachrajda@nrc.ca

- [S1] Y. Komijani, T. Choi, F. Nichele, K. Ensslin, T. Ihn, D. Reuter, and A. D. Wieck, *Phys. Rev. B* **88**, 035417 (2013).
[S2] L. A. Tracy, J. L. Reno, and T. W. Hargett, LANL Report (2015).
[S3] L. A. Tracy, T. W. Hargett, and J. L. Reno, *Appl. Phys. Lett.* **104**, 123101 (2014).
[S4] A. Bogan, S. A. Studenikin, M. Korkusinski, G. C. Aers, L. Gaudreau, P. Zawadzki, A. S. Sachrajda, L. A. Tracy, J. L. Reno, and T. W. Hargett, *Phys. Rev. Lett.* **118**, 167701 (2017).
[S5] D. V. Bulaev and D. Loss, *Phys. Rev. Lett.* **95**, 076805 (2005).
[S6] P. Szumniak, S. Bednarek, B. Partoens, and F. M. Peeters, *Phys. Rev. Lett.* **109**, 107201 (2012).
[S7] S. I. Dorozhkin, *Solid State Commun.* **72**, 211-214 (1989).
[S8] R. Winkler, S. J. Papadakis, E. P. De Poortere, and M. Shayegan, *Phys. Rev. Lett.* **85**, 4574 (2000).
[S9] I. Puerto Gimenez, M. Korkusinski, and P. Hawrylak, *Phys. Rev. B* **76**, 075336 (2007).
[S10] S. N. Shevchenko, S. Ashhab, and F. Nori, *Phys. Reports* **492**, 1 (2010).
[S11] G. Platero and R. Aguado, *Phys. Reports* **395**, 1 (2004).
[S12] J. Villavicencio, I. Maldonado, E. Cota, and G. Platero, *Phys. Rev. B* **88**, 245305 (2013).
[S13] O. N. Jouravlev and Yu. V. Nazarov, *Phys. Rev. Lett.* **96**, 176804 (2006).
[S14] F. Gallego-Marcos, R. Sanchez, and G. Platero, *J. Appl. Phys.* **117**, 112808 (2015).
[S15] D. Q. Wang, O. Klochan, J.-T. Hung, D. Culcer, I. Farrer, D. A. Ritchie, and A. R. Hamilton, *Nano Lett.* **16**, 7685 (2016).
[S16] L. Jacak, P. Hawrylak, and A. Wojs, *Quantum dots*, Springer, Berlin, 1998.